COMPARATIVE ASSESSMENT OF ADAPTIVE-STENCIL FINITE DIFFERENCE SCHEMES FOR HYPERBOLIC EQUATIONS WITH JUMP DISCONTINUITIES

by

Collin C. Otis

B.S.M.E., University of Pittsburgh, 2008

Submitted to the Graduate Faculty of

the Swanson School of Engineering in partial fulfillment

of the requirements for the degree of

Master of Science

University of Pittsburgh

2010

UNIVERSITY OF PITTSBURGH

SWANSON SCHOOL OF ENGINEERING

This thesis was presented

by

Collin C. Otis

It was defended on

July 19, 2010

and approved by

Dr. Peyman Givi, William K. Whiteford Professor of Mechanical Engineering and Materials Science

Dr. Albert C. To, Assistant Professor of Civil and Environmental Engineering

Dr. Catalin S. Trenchea, Assistant Professor of Mathematics

Thesis Advisor: Dr. Peyman Givi, William K. Whiteford Professor of Mechanical Engineering and Materials Science

COMPARATIVE ASSESSMENT OF ADAPTIVE-STENCIL FINITE DIFFERENCE SCHEMES FOR HYPERBOLIC EQUATIONS WITH JUMP DISCONTINUITIES

Collin C. Otis, M.S.

University of Pittsburgh, 2010

High-fidelity numerical solution of hyperbolic differential equations for functions with jump discontinuities presents a particular challenge. In general, fixed-stencil high-order numerical methods are unstable at discontinuities, resulting in exponential temporal growth of dispersive errors (Gibbs phenomena). Schemes utilizing adaptive stencils have shown to be effective in simultaneously providing high-order accuracy and long-time stability. In this Thesis, the elementary formulation of adaptive-stenciling is described in the finite difference context. Basic formulations are provided for three adaptive-stenciling methods: essentially non-oscillatory (ENO), weighted essentially non-oscillatory (WENO), and energy-stable weighted essentially non-oscillatory (ESWENO) schemes. Examples are presented to display some of the relevant properties of these schemes in solving one-dimensional and two-dimensional linear and nonlinear hyperbolic differential equations with discontinuities.

TABLE OF CONTENTS

LIST OF TABLES

LIST OF FIGURES

ACKNOWLEDGMENTS

I sincerely thank Dr. Peyman Givi for his training, advice, and support throughout my graduate studies. I am also indebted to my colleagues at the Laboratory for Computational Transport Phenomena at the University of Pittsburgh, especially Dr. S. Levent Yilmaz, Mr. Mehdi B. Nik, and Mr. Patrick H. Pisciuneri, for their grants of time and effort on my behalf. Many thanks to Dr. J. Philip Drummond and Dr. Mark H. Carpenter at the NASA Langley Research Center and Dr. M. Reza Sheikhi at Northeastern University for their support. I also thank the members of my thesis defense committee, Dr. Albert C. To and Dr. Catalin S. Trenchea.

This work is supported by the NASA Aeronautics Research Mission Directorate (ARMD) 2008 Aeronautics Graduate Scholarship Program. Additional support for this work is provided by the U.S. National Center for Hypersonic Combined Cycle Propulsion under NASA/AFOSR Grant FA9550-09-1-0611.

I dedicate this work to my wife, Audra, for her love and support throughout all my endeavors.

1.0 INTRODUCTION

High-fidelity numerical solution of hyperbolic differential equations for functions with jump discontinuities presents a particular challenge. In general, fixed-stencil high-order numerical methods are unstable at discontinuities, resulting in exponential temporal growth of dispersive errors (Gibbs phenomena[1,2]). These errors are exemplified in Fig. 2, which shows the MacCormack scheme[3] (second-order in space and time) solution of a one-dimensional step wave traveling to the right. The transport and growth of dispersive errors significantly pollutes the solution and often renders the results completely useless. This numerical instability can be remediated if a dissipative numerical scheme is used; however, this degrades the accuracy. Due to these considerations, accurate solution of problems with discontinuities requires further research. One such problem is associated with supersonic flows.[4] In scramjets, for example, shock diamonds exist throughout the domain. These shocks have a significant effect on mixing and subsequent chemical reaction, which, in-turn, drastically affects the hydrodynamics.[5] To simulate the jump discontinuities and accurately account for the coupling of physics and chemical reaction requires highly accurate and stable numerical methods. In recent years, *adaptive-stencil* schemes have become popular for solution of such problems.[6–9] These schemes bias the finite difference stencil away from the discontinuity, resulting in a greater numerical stability. In this Thesis, we consider three such methods: *essentially non-oscillatory* (ENO),[10] *weighted essentially non-oscillatory* (WENO),[11,12] and *energy-stable weighted essentially non-oscillatory* (ESWENO)[13] schemes.

2.0 FINITE DIFFERENCE FORMULATION

2.1 BASIC FORMULATION IN ONE DIMENSION

Our objective is to solve the one-dimensional hyperbolic equation

$$\frac{\partial u}{\partial t} + \frac{\partial f}{\partial x} = 0 \tag{2.1}$$

using finite difference methods on the domain $x \in [a, b]$, $t \in [0, \infty)$ for the piecewise continuous functions $u = u(x, t)$ and $f = f(x, t)$, where x and t denote space and time, respectively. In this work we are primarily concerned with approximation of the spatial derivative,

$$f_x = \frac{\partial f}{\partial x}, \tag{2.2}$$

therefore, we march forward in time using the simple first-order discretization,

$$u^{(n+1)} = u^{(n)} - \Delta t \frac{\partial f^{(n)}}{\partial x} + O(\Delta t), \tag{2.3}$$

where $u^{(n)}$ denotes $u(x, n\Delta t)$, $n = 0, 1, ...$. To compute f_x, the domain is discretized via $N + 1$ evenly-spaced *half-points*,

$$a = x_{\frac{1}{2}} < x_{\frac{3}{2}} < ... < x_{N-\frac{1}{2}} < x_{N+\frac{1}{2}} = b, \tag{2.4}$$

with *cells*, *grid-points*, and *grid-spacing* given by

$$\begin{aligned} I_i &\equiv \left[x_{i-\frac{1}{2}}, x_{i+\frac{1}{2}}\right] , \\ x_i &\equiv \frac{1}{2}\left(x_{i-\frac{1}{2}} + x_{i+\frac{1}{2}}\right) , \\ \Delta x &\equiv x_{i+\frac{1}{2}} - x_{i-\frac{1}{2}} , \qquad i = 1, 2, ..., N . \end{aligned} \tag{2.5}$$

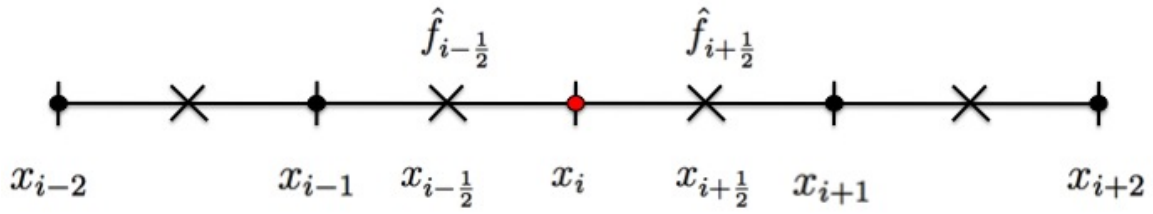

Figure 1: Example of a finite difference discretization centered at grid-point x_i. Grid-points, half-points, and numerical fluxes are shown.

Figure 1 shows an example of this discretization notation near the point x_i. Given the point values $f_i \equiv f(x_i)$, $i = 1, 2, ..., N$, we wish to construct a *numerical flux*, $\hat{f}$ (see Fig. 1), such that the kth order approximation of the derivative at the grid-point, x_i, of cell I_i is given by

$$\frac{1}{\Delta x}\left(\hat{f}_{i+\frac{1}{2}} - \hat{f}_{i-\frac{1}{2}}\right) = f_x(x_i) + O(\Delta x^k)\,, \qquad i = 1, 2, ..., N\,. \tag{2.6}$$

We begin by choosing a *stencil*, S_i, at the point x_i, based on the point x_i itself, r points to the left of x_i, and s points to the right of x_i,

$$S_i = \{x_{i-r}, ..., x_{i+s}\}, \tag{2.7}$$

with $r, s \geq 0$ and $r + s + 1 = k$. We seek a flux, $\hat{f}$, that is a function of the projection of f onto the stencil S_i,

$$\hat{f}_{i+\frac{1}{2}} = \hat{f}(f_{i-r}, ..., f_{i+s})\,, \qquad i = 0, 1, ..., N\,. \tag{2.8}$$

If a function $h(x)$ can be found such that

$$f(x) = \frac{1}{\Delta x}\int_{x-\frac{\Delta x}{2}}^{x+\frac{\Delta x}{2}} h(\eta)d\eta, \tag{2.9}$$

then

$$f_x(x) = \frac{1}{\Delta x}\left[h\left(x + \frac{\Delta x}{2}\right) - h\left(x - \frac{\Delta x}{2}\right)\right]\,. \tag{2.10}$$

Comparing Eqs. (2.6) and (2.10), we choose the flux function to be

$$\hat{f}_{i+\frac{1}{2}} = h\left(x_{i+\frac{1}{2}}\right) + O(\Delta x^k)\,. \tag{2.11}$$

It would seem that an $O(\Delta x^{k+1})$ term is needed in Eq. (2.11) to recover Eq. (2.6), due to the $\frac{1}{\Delta x}$ multiplier in Eq. (2.10). In practice, however, the $O(\Delta x^k)$ term in Eq. (2.11) is typically smooth.[14] Hence, the difference in Eq. (2.6) yields an extra $O(\Delta x)$ term that cancels the Δx term in the denominator. It is not easy to evaluate Eq. (2.9) for h, as it is only implicitly defined. It is shown in Ref. [14] that a kth order approximation to h can be computed from a linear combination of the k point values in the stencil, S_i,

$$h\left(x_{i+\frac{1}{2}}\right) = \sum_{j=0}^{k-1} c_{rj} f_{i-r+j} + O(\Delta x^k), \qquad h\left(x_{i-\frac{1}{2}}\right) = \sum_{j=0}^{k-1} \tilde{c}_{rj} f_{i-r+j} + O(\Delta x^k) \tag{2.12}$$

where c_{rj} and $\tilde{c}_{rj}$ are constants. Substituting Eq. (2.12) into Eq. (2.11) yields

$$\hat{f}^-_{i+\frac{1}{2}} = \sum_{j=0}^{k-1} c_{rj} f_{i-r+j}, \qquad \hat{f}^+_{i-\frac{1}{2}} = \sum_{j=0}^{k-1} \tilde{c}_{rj} f_{i-r+j} \tag{2.13}$$

where the superscripts $\pm$ are due to the possibility of different stencils at points x_i and x_{i+1}. By symmetry, it is apparent that

$$\tilde{c}_{rj} = c_{r-1,j}. \tag{2.14}$$

The stencil coefficients, c_{rj}, are given in Table 1 for $k = 1, 2, ..., 5$. The numerical flux in Eq. (2.6) is recovered from Eq. (2.13) via

$$\hat{f}_{i+\frac{1}{2}} = m\left(\hat{f}^+_{i+\frac{1}{2}}, \hat{f}^-_{i+\frac{1}{2}}\right) \tag{2.15}$$

where the function m is a monotone flux satisfying certain properties.[14] There are many possibilities for m. In this work we limit ourselves to the Lax-Friedrichs flux,[15]

$$m(a, b) = \frac{1}{2}\left[f(a) + f(b) - \alpha(b - a)\right], \tag{2.16}$$

where

$$\alpha = \max_u \left|\frac{\partial f}{\partial u}\right|. \tag{2.17}$$

The Lax-Friedrichs flux is implemented by first splitting the physical fluxes at each grid point into right-moving and left-moving waves via

$$f^\pm_i = \frac{1}{2}(f_i \pm \alpha u_i). \tag{2.18}$$

Table 1: Stencil coefficients, c_{rj}, in Eq. (2.13)

k	r	j=0	j=1	j=2	j=3	j=4
1	-1	1				
	0	1				
2	-1	3/2	-1/2			
	0	1/2	1/2			
	1	-1/2	3/2			
3	-1	11/6	-7/6	1/3		
	0	1/3	5/6	-1/6		
	1	-1/6	5/6	1/3		
	2	1/3	-7/6	11/6		
4	-1	25/12	-23/12	13/12	-1/4	
	0	1/4	13/12	-5/12	1/12	
	1	-1/12	7/12	7/12	-1/12	
	2	1/12	-5/12	13/12	1/4	
	3	-1/4	13/12	-23/12	25/12	
5	-1	137/60	-163/60	137/60	-21/20	1/5
	0	1/5	77/60	-43/60	17/60	-1/20
	1	-1/20	9/20	47/60	-13/60	1/30
	2	1/30	-13/60	47/60	9/20	-1/20
	3	-1/20	17/60	-43/60	77/60	1/5
	4	1/5	-21/20	137/60	-163/60	137/60

The $\pm$ numerical fluxes at the half-points are reconstructed as

$$\hat{f}^{-}_{i+\frac{1}{2}} = \sum_{j=0}^{k-1} c_{rj} f^{+}_{i-r+j}, \qquad \hat{f}^{+}_{i-\frac{1}{2}} = \sum_{j=0}^{k-1} \tilde{c}_{rj} f^{-}_{i-r+j}. \tag{2.19}$$

Finally, the numerical flux is computed as

$$\hat{f}_{i+\frac{1}{2}} = \hat{f}^{+}_{i+\frac{1}{2}} + \hat{f}^{-}_{i+\frac{1}{2}}, \tag{2.20}$$

yelding the desired Lax-Friedrichs flux.

2.2 FIXED-STENCIL APPROXIMATION

In fixed stencil approximations, the left shift r and the right shift s do not change with location i. Fixed-stencil central and biased difference schemes can be recovered from Eq. (2.13) and Table 1. For example, the traditional first-order upwind-biased scheme,[16,17]

$$\frac{\partial f}{\partial x} = \begin{cases} \frac{f_i - f_{i-1}}{\Delta x} : & u > 0 \\ \frac{f_{i+1} - f_i}{\Delta x} : & u \leq 0 \end{cases}, \tag{2.21}$$

is recovered from the numerical flux reconstruction procedure using $k = 1$, and

$$r = \begin{cases} 1 : & u > 0 \\ 0 : & u \leq 0. \end{cases} \tag{2.22}$$

2.3 ESSENTIALLY NON-OSCILLATORY (ENO) SCHEMES

The *essentially non-oscillatory* (ENO) methodology, first introduced by Harten, *et al.*,[10] involves the use of an adaptive-stenciling procedure to avoid inclusion of cells with discontinuities in the stencil. This is achieved by "sensing" discontinuities using Newton undivided differences and altering the left shift, r, to bias the stencil away from the discontinuity. We begin by calculating the Newton undivided differences, F_{ij}, on the entire domain, where

$$F_{i0} = f_i \tag{2.23}$$

$$F_{ij} = F_{(i+1)(j-1)} - F_{i(j-1)}\,, \qquad j = 1, 2, ..., k \tag{2.24}$$

To form the stencil S_i, we seek to assemble the set of k consecutive points, which must include the point x_i, such that $f(x)$ is "smoothest" on this stencil as compared to the other $k-1$ possible stencils. We begin the stencil assembly process with only the point x_i in the stencil,

$$S_i^{(1)} = x_i, \tag{2.25}$$

and add one point at a time until the stencil is filled. The second point in S_i is chosen by comparing the first undivided differences at x_{i-1} and x_{i+1} and adding the point with the smaller absolute-valued Newton undivided difference, $|F_{j1}|$, to S_i. Subsequent points are added to the stencil by comparing the higher-order Newton undivided differences of the left and the right neighbors of the partially constructed stencil. In general, the jth point is chosen as

$$x_j = \begin{cases} x_{r'}: & |F_{(i-1)j}| < |F_{ij}| \\ x_{s'}: & |F_{(i-1)j}| \geq |F_{ij}| \end{cases} \tag{2.26}$$

where r' and s' are the indices of the left and right neighbors of the partially constructed stencil. Once the stencil is chosen at each grid-point, the reconstruction procedure in section 2.1 is carried out using the appropriate stencil coefficients, c_{rj}, chosen from Table 1.

2.4 WEIGHTED ESSENTIALLY NON-OSCILLATORY (WENO) SCHEMES

Instead of using the smoothest stencil at point x_i, *weighted essentially non-oscillatory* (WENO)[11,12] schemes use a convex combination of all k possible stencils. This increases the accuracy to $O(\Delta x^{2k-1})$ in regions where the solution is smooth, while maintaining ENO biasing near discontinuities. To compute the numerical flux, WENO schemes utilize a weighted combination of the k different reconstructions of the value $\hat{f}_{i+\frac{1}{2}}$. Equation (2.13) is used to evaluate

$$\hat{f}^{-\,(r)}_{i+\frac{1}{2}} = \sum_{j=0}^{k-1} c_{rj} f_{i-r+j}, \qquad \hat{f}^{+\,(r)}_{i-\frac{1}{2}} = \sum_{j=0}^{k-1} \tilde{c}_{rj} f_{i-r+j}, \qquad r = 0, ..., k-1, \tag{2.27}$$

and a convex combination of all $\hat{f}^{\pm\,(r)}_{i+\frac{1}{2}}$, $r = 0, ..., k-1$ is taken,

$$\hat{f}^{-}_{i+\frac{1}{2}} = \sum_{r=0}^{k-1} \omega_r \hat{f}^{-\,(r)}_{i+\frac{1}{2}}, \qquad \hat{f}^{+}_{i-\frac{1}{2}} = \sum_{r=0}^{k-1} \tilde{\omega}_r \hat{f}^{+\,(r)}_{i-\frac{1}{2}}, \tag{2.28}$$

using weights ω_r and $\tilde{\omega}_r$ with the constraints

$$\tilde{\omega_r},\, \omega_r \geq 0, \qquad \sum_{r=0}^{k-1} \omega_r = \sum_{r=0}^{k-1} \tilde{\omega}_r = 1. \tag{2.29}$$

It is apparent that if the function is smooth in all k candidate stencils, there exist the constants d_r, called *target weights* (see Table 2), such that

$$\hat{f}_{i+\frac{1}{2}} = \sum_{r=0}^{k-1} d_r \hat{f}^{\,(r)}_{i+\frac{1}{2}} = \hat{f}\left(x_{i+\frac{1}{2}}\right) + O(\Delta x^{2k-1}). \tag{2.30}$$

Clearly, we would like the weights, ω_r and $\tilde{\omega}_r$, to recover this $O(\Delta x^{2k-1})$ accuracy in regions where f is smooth. These considerations lead to the weights:[14]

$$\omega_r = \frac{\alpha_r}{\sum_{s=0}^{k-1} \alpha_s}, \qquad \tilde{\omega}_r = \frac{\tilde{\alpha_r}}{\sum_{s=0}^{k-1} \tilde{\alpha}_s} \tag{2.31}$$

with

$$\alpha_r = \frac{d_r}{\epsilon + {\beta_r}^2}, \qquad \tilde{\alpha}_r = \frac{\tilde{d}_r}{\epsilon + {\beta_r}^2} \tag{2.32}$$

where, by symmetry,

$$\tilde{d}_r = d_{k-1-r} \tag{2.33}$$

Table 2: Target weights, d_r, in Eq. (2.30)

k	$r=0$	$r=1$	$r=2$
1	1		
2	$\frac{2}{3}$	$\frac{1}{3}$	
3	$\frac{3}{10}$	$\frac{3}{5}$	$\frac{1}{10}$

and $\epsilon > 0$ is a small number used to prevent a zero denominator. We take $\epsilon = 10^{-6}$ as suggested in Ref. [12]. The parameters β_r are *smooth indicators* given by

$$\begin{aligned} \beta_0 &= (f_{i+1} - f_i)^2 \\ \beta_1 &= (f_i - f_{i-1})^2 \end{aligned} \tag{2.34}$$

for third order WENO ($k = 2$) and

$$\begin{aligned} \beta_0 &= \frac{13}{12}(f_i - 2f_{i+1} + f_{i+2})^2 + \frac{1}{4}(3f_i - 4f_{i+1} + f_{i+2})^2 \\ \beta_1 &= \frac{13}{12}(f_{i-1} - 2f_i + f_{i+1})^2 + \frac{1}{4}(f_{i-1} - f_{i+1})^2 \\ \beta_2 &= \frac{13}{12}(f_{i-2} - 2f_{i-1} + f_i)^2 + \frac{1}{4}(f_{i-2} - 4f_{i-1} + 3f_i)^2 \end{aligned} \tag{2.35}$$

for fifth order WENO ($k = 3$).

2.5 ENERGY-STABLE WENO (ESWENO) SCHEMES

While ENO and WENO schemes are robust, their discrete spatial derivative operators do not satisfy the summation by parts (SBP) rule.[18,19] Therefore, generalized stability of these schemes cannot be shown.[13] The *energy-stable weighted essentially non-oscillatory* (ESWENO)[13] scheme is a modification of the WENO scheme to explicitly provide stability in the energy norm by requiring that the discrete spatial derivative operator satisfies

SBP.[13,20,21] The ESWENO scheme utilizes modifications of α_r (and $\tilde{\alpha}_r$) in the weight functions, Eq. (2.32), to satisfy SBP:

$$\alpha_r = d_r \left(1 + \frac{\tau}{\epsilon + \beta_r} \right), \tag{2.36}$$

where

$$\tau = \begin{cases} (f_{i+1} - 2f_i + f_{i-1})^2 & : k = 2 \\ (f_{i-2} - 4f_{i-1} + 6f_i - 4f_{i+1} + f_{i+2})^2 & : k = 3 \end{cases}. \tag{2.37}$$

ESWENO schemes also utilize a modified numerical flux given by

$$\hat{f}^{(ES)}_{i+\frac{1}{2}} = \hat{f}_{i+\frac{1}{2}} + \hat{f}^{(D)}_{i+\frac{1}{2}}, \tag{2.38}$$

where $\hat{f}^{(D)}_{i+\frac{1}{2}}$ is a dissipative term added to guarantee stability:

$$\begin{aligned} \hat{f}^{(D)}_{i+\frac{1}{2}} &= \left(\mu_{i+1} + \frac{\omega_{1,i+\frac{3}{2}} - \omega_{1,i+\frac{1}{2}}}{8} \right) (f_i - f_{i+1}), \\ \mu_i &= \frac{1}{8} \sqrt{\left(\omega_{1,i+\frac{1}{2}} - \omega_{1,i-\frac{1}{2}} \right)^2 + \delta^2}, \\ \delta &= \left(\frac{1}{N} \right)^2. \end{aligned} \tag{2.39}$$

2.6 EXTENSION TO TWO DIMENSIONS

Two-dimensional reconstruction requires a straightforward component-wise application of the one-dimensional procedures above. For example, the derivative, w_x, of a function, $w = w(x, y)$ is computed by fixing $y = y_j$ and utilizing the one-dimensional reconstruction procedure above in the x-direction, substituting $w(x, y_j)$ for f. A similar procedure is followed to compute w_y.

3.0 NUMERICAL TESTS

Numerical calculations are performed to comparatively assess the ENO, WENO, and ESWENO methodologies. Fixed-stencil cases are also considered for comparison. For fixed-stencil calculations, spatial derivatives at the boundaries are calculated using interior-biased stencils with the same accuracy as that within the domain interior. For adaptive-stencil calculations, stencil-biasing is reduced at the boundaries to include only stencils that lie within the domain. Time discretization is first-order explicit (see Eq. (2.3)) for all cases except for the MacCormack scheme.[3] This scheme is second-order in time and space. A time step of $\Delta t = 0.001$ is used for all cases, which satisfies the CFL condition.[22]

3.1 ONE-DIMENSIONAL CASES

All one-dimensional simulations are conducted over the spatial domain $x \in [-1, 1]$ on a uniform Cartesian grid using $N = 40$ grid points and $t \in [0, 2]$.

3.1.1 LINEAR SCALAR WAVE EQUATION

The one-dimensional form of the linear scalar wave equation for a right-moving step is given by

$$\begin{aligned} \frac{\partial c}{\partial t} + u\frac{\partial c}{\partial x} &= 0, \quad u = 0.25, \\ c(x,0) &= \begin{cases} 1 & : \quad x < -0.5 \\ 0 & : \quad x \geq -0.5 \end{cases} \\ c(0,t) &= 1 \end{aligned} \tag{3.1}$$

for scalar $c = c(x,t)$. Because information propagates only in the positive x-direction, the boundary value $c(1,t)$ is calculated using the conservation equation in Eq. (3.1) with an interior-biased stencil. Calculations are performed using the MacCormack scheme (Fig. 2), kth order ($k = 1, ..., 5$) upwind-biased, fixed-stencil schemes (Fig. 3), and kth order ($k = 3, 5$) ENO, WENO, and ESWENO schemes (Fig. 4). The results are compared with the exact solution at $t = 2$. As expected, the MacCormack scheme displays large dispersive errors caused by the large gradient at the discontinuity. In the remaining fixed-stencil schemes, upwinding is used to improve stability. The two-point-biased, even-ordered ($k = 2p$, $p = 1, 2$) schemes display significant dispersive errors. The second-order results are shown. Higher even-ordered schemes portray even greater instability; thus, they are not presented. The first-order results do not display any noticeable instabilities due to their large numerical dissipation. However, this degrades accuracy near the discontinuity. The results of the higher odd-ordered ($k = 2p - 1$, $p = 2, 3$) schemes display the Gibbs phenomena near the discontinuity. The adaptive-stencil schemes (ENO, WENO, and ESWENO), on the other hand, do not display significant dispersive errors. By visual inspection, the diffusive error is design-order and the fifth-order scheme is clearly less dissipative than the third-order scheme.

3.1.2 INVISCID BURGERS' EQUATION

The one-dimensional form of the inviscid Burgers' equation[23] for a right-moving step is given by

$$\begin{aligned} \frac{\partial u}{\partial t} + u\frac{\partial u}{\partial x} &= 0, \\ u(x,0) &= \begin{cases} 1 & : \quad x < -0.5 \\ 0 & : \quad x \geq -0.5 \end{cases} \\ u(0,t) &= 1 \end{aligned} \tag{3.2}$$

for the velocity $u = u(x,t)$. Because information propagates only in the positive x-direction, the boundary value $u(1,t)$ is calculated using the conservation equation in Eq. (3.2) with an interior-biased stencil. Calculations are performed for the third-order, upwind-biased fixed

stencil scheme and third-order and fifth-order ENO, WENO, and ESWENO schemes. The computed results are compared with the exact solution at $t = 2$ in Fig. 5 and show good agreements. All schemes show smaller diffusive errors than those in the linear case. The third-order fixed-stencil scheme displays the Gibbs phenomena near the discontinuity. The adaptive-stencil methods show no noticeable dispersive errors.

3.2 TWO-DIMENSIONAL CASES

All two-dimensional simulations are performed on the spatial domain $x, y \in [-1, 1]$ on a uniform Cartesian $N_x \times N_y$ grid using $N_x = N_y = 100$ grid-points.

3.2.1 LINEAR SCALAR WAVE EQUATION

The two-dimensional form of the linear scalar wave equation for a counterclockwise solid-body rotation is given by

$$\begin{aligned} \frac{\partial c}{\partial t} + u\frac{\partial c}{\partial x} + v\frac{\partial c}{\partial y} &= 0 \\ u = -\omega y, \quad v = \omega x, \quad \omega &= 0.25 \end{aligned} \tag{3.3}$$

for the scalar field $c = c(x, y, t) \in [0, 1]$. The initial condition is shown in Fig. 6. The Dirichlet boundary condition $c = 0$ is imposed if flow is entering the domain; otherwise, the boundary values are calculated using interior-biased stencils. Calculations are performed for upwind-biased fixed-stencil schemes. However, only the first-order scheme is stable enough to complete one rotation. Calculations are also performed for third-order and fifth-order ENO, WENO, and ESWENO schemes. The two-dimensional contours of c are presented and one-dimensional plots of c at $y = -0.09$ are compared with the exact solution after one rotation in Figs. 7 - 9 . While the fixed-stencil calculation remains stable, the large numerical dissipation results in a final solution that bears little resemblance to the exact solution. The ENO, WENO, and ESWENO schemes also remain stable; however, the third-order WENO scheme displays much greater numerical diffusion than the ENO and ESWENO schemes.

The fifth-order results are more accurate and show very good agreements with the exact solution, although the ESWENO results show slight dispersive errors in the discontinuous region.

3.2.2 INVISCID BURGERS' EQUATION

The incompressible form of the two-dimensional inviscid Burgers' equation is given by

$$\frac{\partial \mathbf{U}}{\partial t} + \frac{\partial \mathbf{F}}{\partial x} + \frac{\partial \mathbf{G}}{\partial y} = 0, \tag{3.4}$$

where

$$\mathbf{U} = \begin{bmatrix} u \\ v \end{bmatrix}, \quad \mathbf{F} = \begin{bmatrix} u^2 \\ uv \end{bmatrix}, \quad \mathbf{G} = \begin{bmatrix} uv \\ v^2 \end{bmatrix}$$

and $u = u(x, y, t)$ and $v = v(x, y, t)$ are the components of the velocity in the x and y directions, respectively. The initial condition for u and v is shown in Fig. 10. The Dirichlet boundary condition $u = v = 0$ is imposed if flow is entering the domain; otherwise the boundary values are calculated using interior-biased stencils. The Lax-Friedrichs flux-splitting procedure is modified to accommodate a system of equations. A flux-splitting similar to Eq. (2.18) is used:

$$F_i^{\pm} = \frac{1}{2}(F_i \pm \alpha_F u) \tag{3.5}$$

with

$$\alpha_F = \max_u \max_j |\lambda_j| \tag{3.6}$$

where λ_j are the eigenvalues of the Jacobian $\partial F_i / \partial U_j$. The reconstruction procedure is performed for each component of F_i^+ and F_i^- separately according to Eq. (2.19) and the numerical flux is computed from Eq. (2.20). A similar procedure is performed to compute the fluxes $G_i^{\pm}$. Two-dimensional contours of u are presented at $t = 0.5$ for the first-order fixed-stencil upwind-biased scheme (Fig. 11) and third-order and fifth-order ENO, WENO, and ESWENO schemes (Fig. 12). Higher-order fixed-stencil schemes are found to be unstable; therefore, their results are not presented here. The adaptive-stencil schemes are stable and show acceptable diffusive errors. Slight oscillations of unknown origin are apparent in the fifth-order ENO results.

4.0 RESULTS

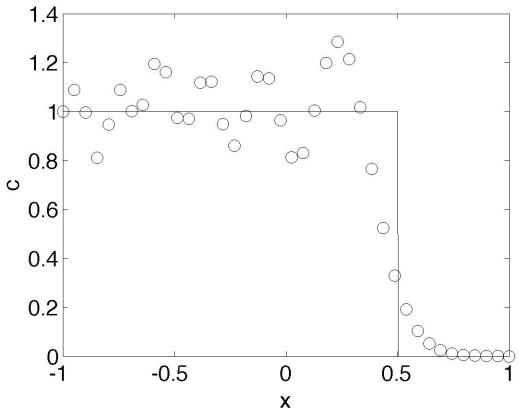

Figure 2: MacCormack scheme solution for one-dimensional linear scalar wave equation at $t = 2$. ($\circ$) numerical solution, (——) exact solution.

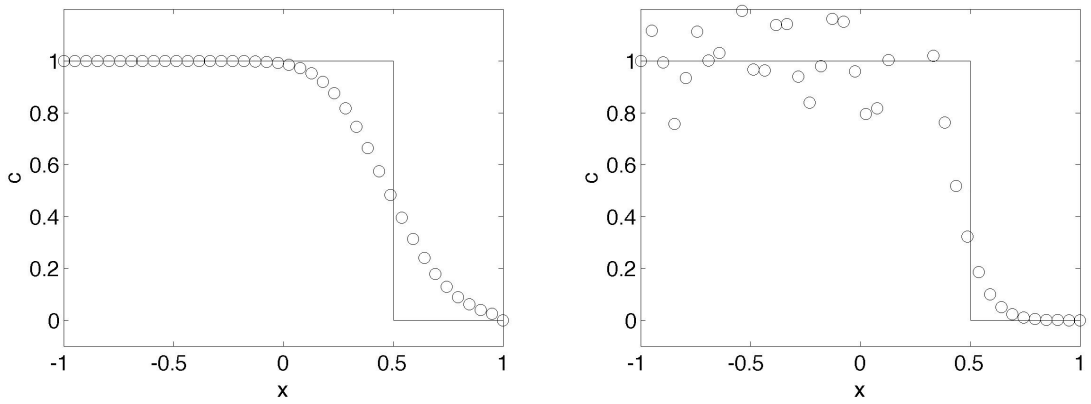

(a) First-order

(b) Second-order

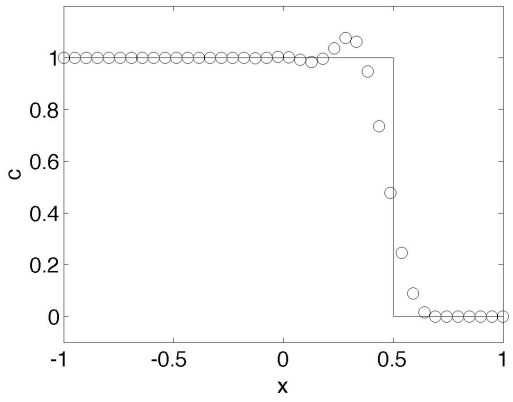

(c) Third-order

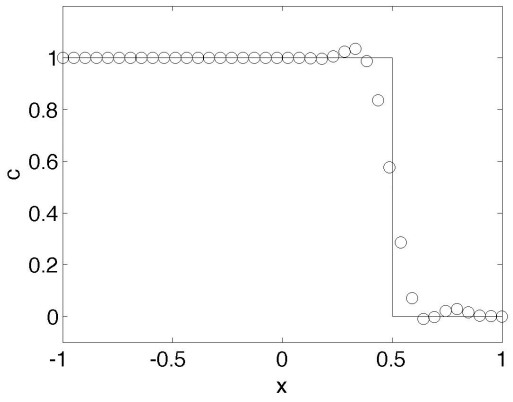

(d) Fifth-order

Figure 3: Upwind-biased fixed-stencil scheme solutions for one-dimensional linear scalar wave equation at $t = 2$. ($\circ$) numerical solution, (——) exact solution.

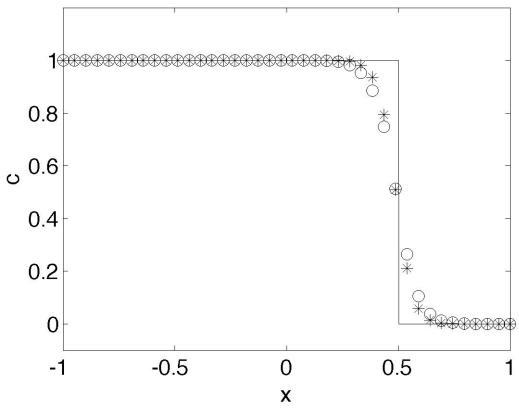

(a) ENO

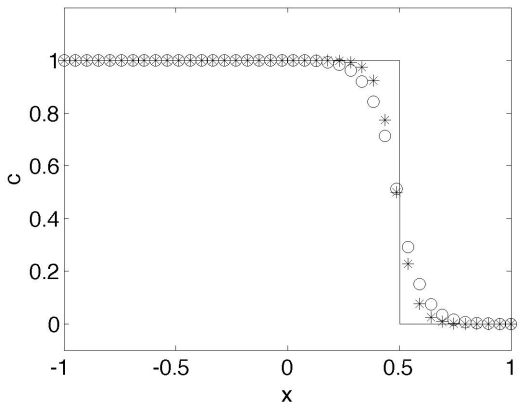

(b) WENO

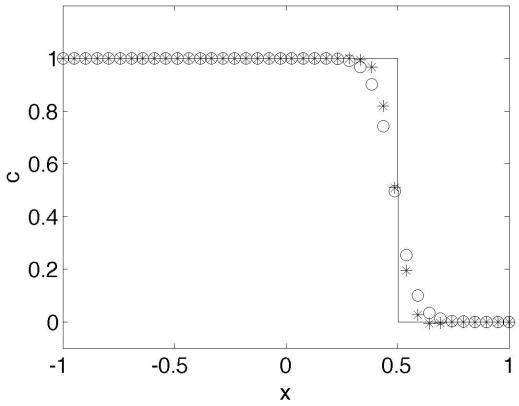

(c) ESWENO

Figure 4: Adaptive-stencil scheme solutions for one-dimensional linear scalar wave equation at $t = 2$. ($\circ$) third-order numerical solution, ($*$) fifth-order numerical solution, (——) exact solution.

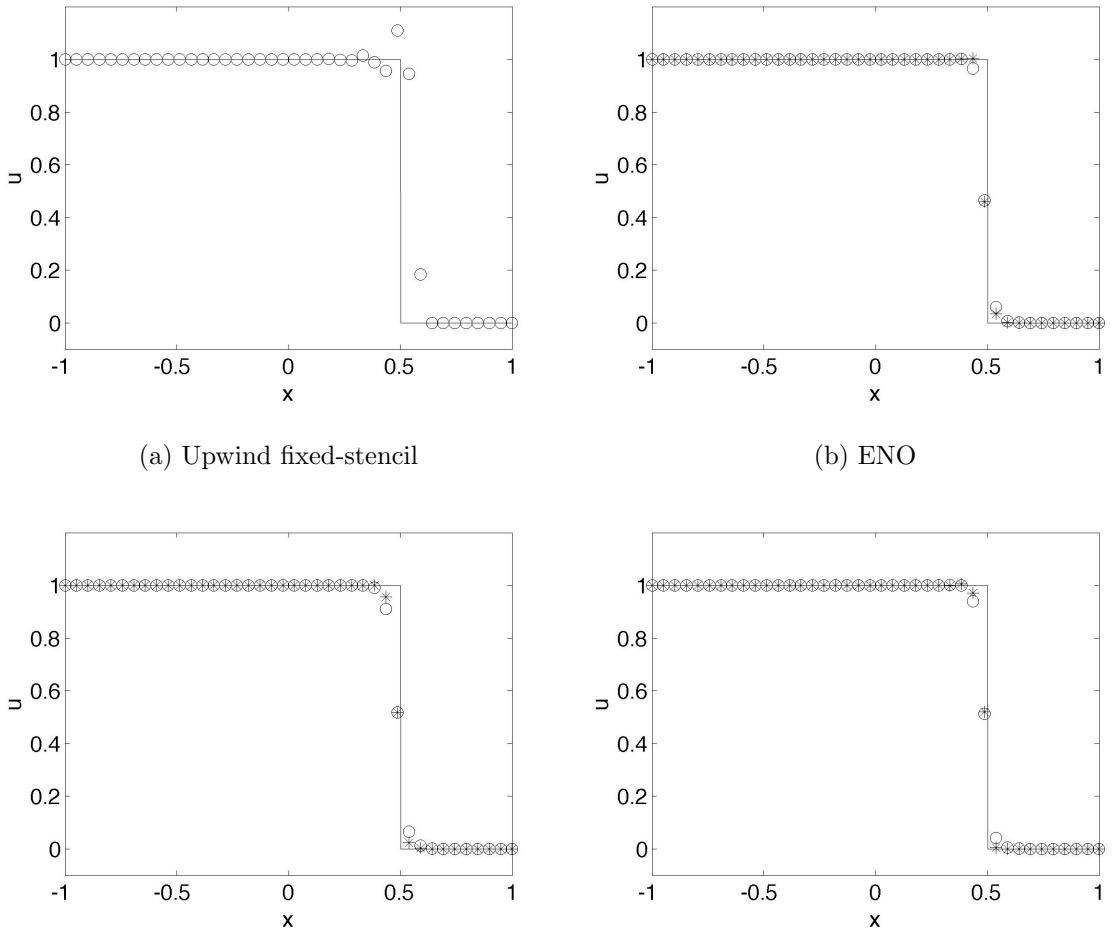

(a) Upwind fixed-stencil

(b) ENO

(c) WENO

(d) ESWENO

Figure 5: Solutions for one-dimensional inviscid Burgers' equation at $t = 2$. ($\circ$) third-order numerical solution, ($*$) fifth-order numerical solution, (——) exact solution.

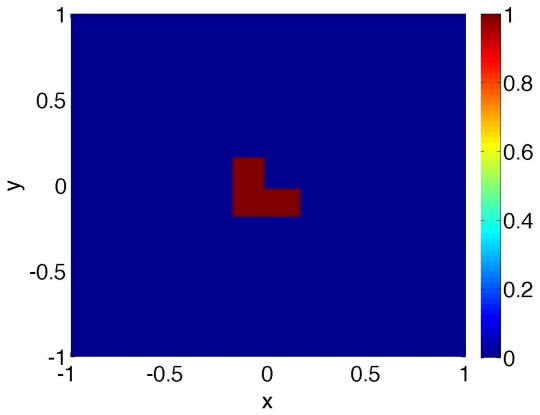

Figure 6: Initial condition, $c(x, y, 0)$, for two-dimensional linear scalar wave equation.

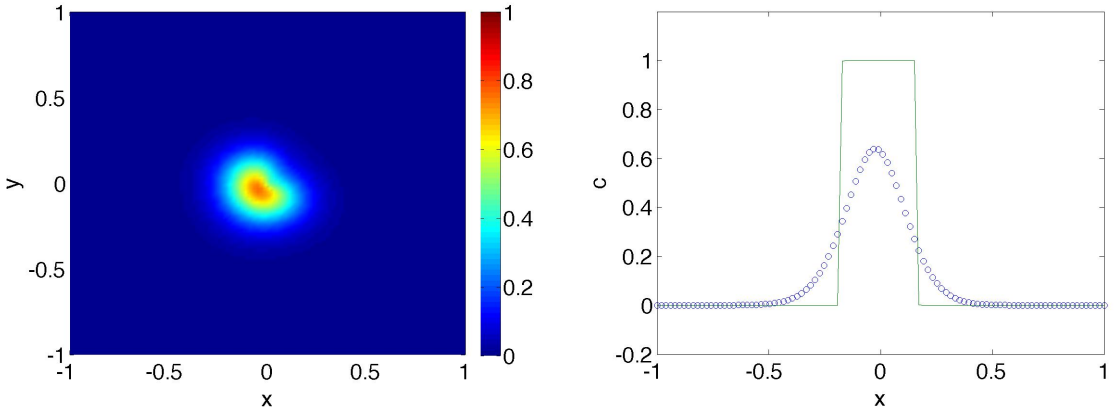

(a) Two-dimensional contour

(b) Cross-section at $y = -0.09$. ($\circ$) numerical solution, (——) exact solution.

Figure 7: First-order upwind-biased fixed-stencil c solution for two-dimensional linear scalar wave equation after one rotation.

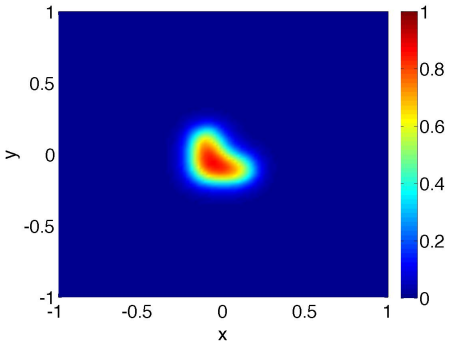

(a) ENO two-dimensional contour.

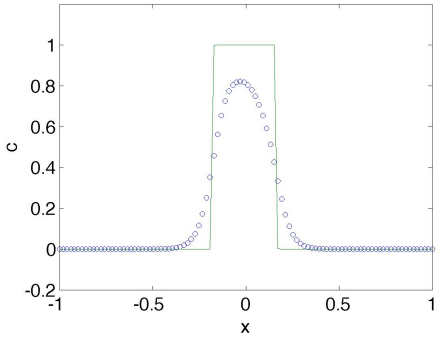

(b) ENO cross-section at $y = -0.09$. ($\circ$) numerical solution, (——) exact solution.

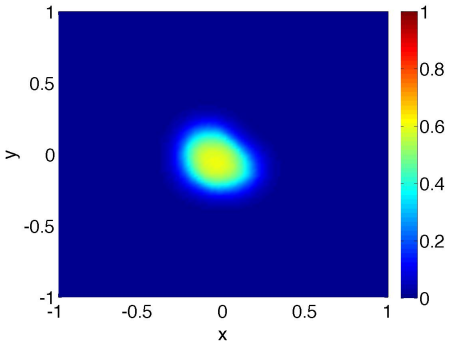

(c) WENO two-dimensional contour.

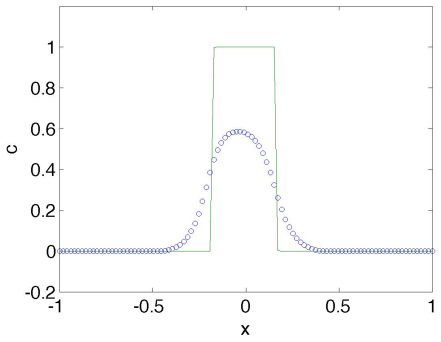

(d) WENO cross-section at $y = -0.09$. ($\circ$) numerical solution, (——) exact solution.

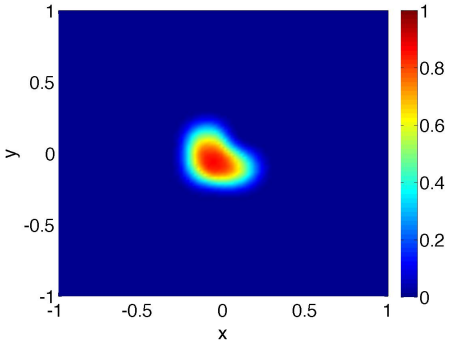

(e) ESWENO two-dimensional contour.

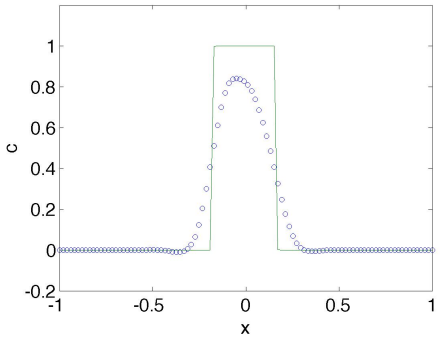

(f) ESWENO cross-section at $y = -0.09$. ($\circ$) numerical solution, (——) exact solution.

Figure 8: Third-order adaptive-stencil c solutions for two-dimensional linear scalar wave equation after one rotation.

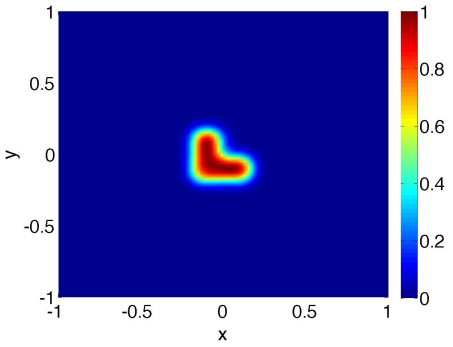

(a) ENO two-dimensional contour.

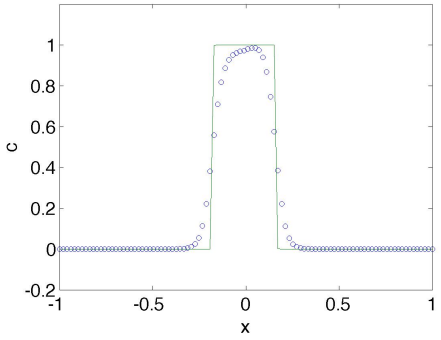

(b) ENO cross-section at $y = -0.09$. ($\circ$) numerical solution, (——) exact solution.

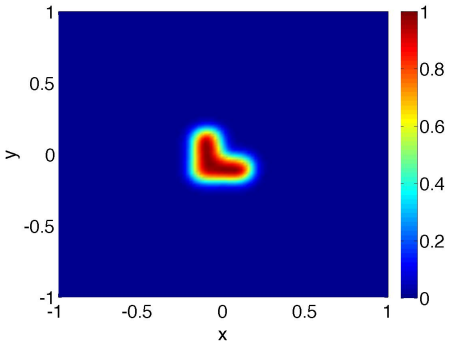

(c) WENO two-dimensional contour.

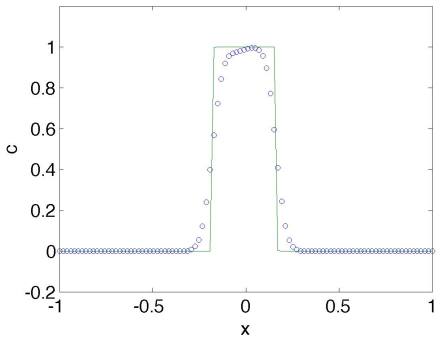

(d) WENO cross-section at $y = -0.09$. ($\circ$) numerical solution, (——) exact solution.

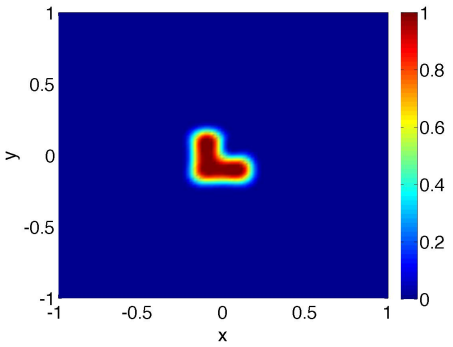

(e) ESWENO two-dimensional contour.

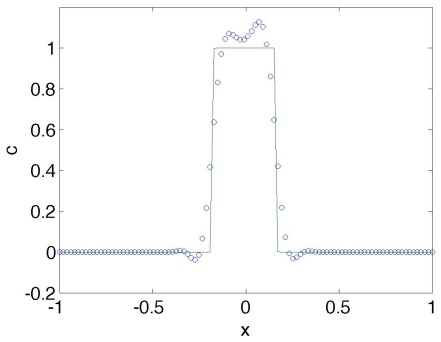

(f) ESWENO cross-section at $y = -0.09$. ($\circ$) numerical solution, (——) exact solution.

Figure 9: Fifth-order adaptive-stencil c solutions for two-dimensional linear scalar wave equation after one rotation.

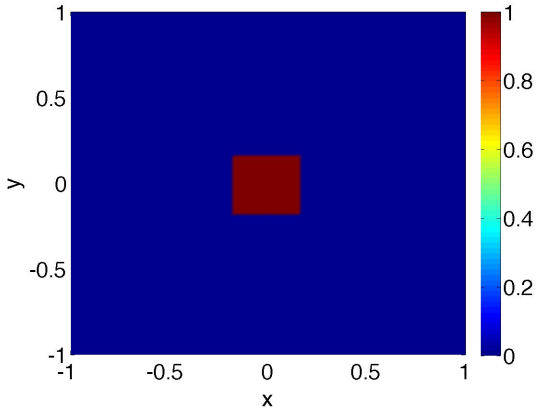

Figure 10: Initial condition for velocity components u and v for two-dimensional inviscid Burgers' equation.

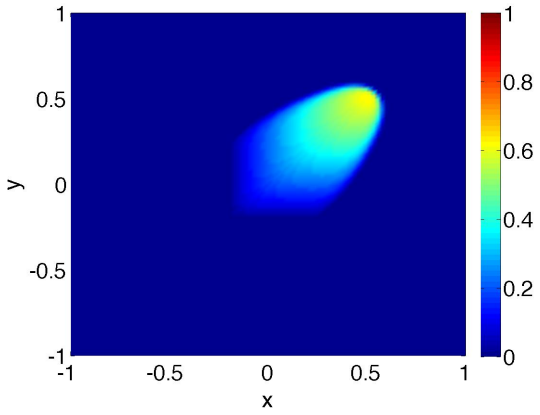

Figure 11: First-order upwind-biased fixed-stencil u-velocity solution for two-dimensional inviscid Burgers' equation at $t = 0.5$.

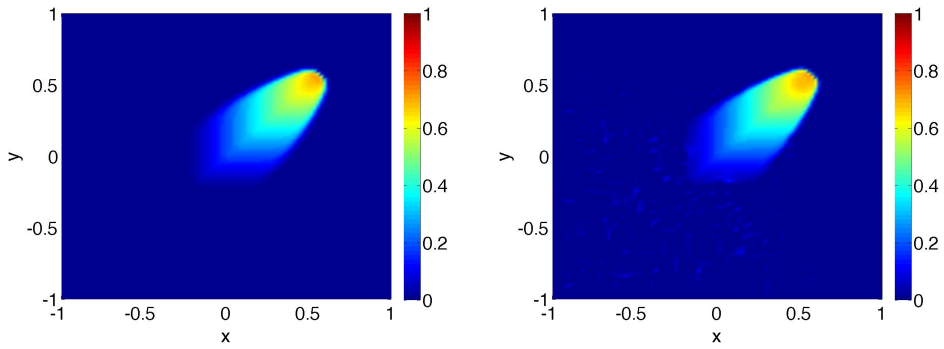

(a) Third-order ENO

(b) Fifth-order ENO

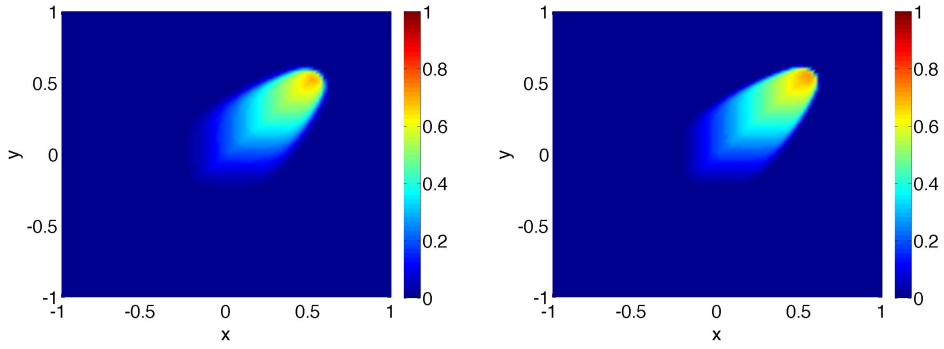

(c) Third-order WENO

(d) Fifth-order WENO

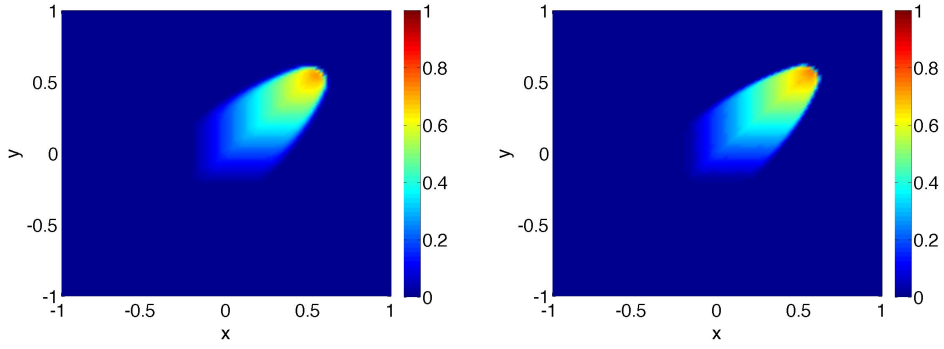

(e) Third-order ESWENO

(f) Fifth-order ESWENO

Figure 12: Adaptive-stencil u-velocity solutions for two-dimensional inviscid Burgers' equation at $t = 0.5$.

5.0 CONCLUSIONS

For the high-order numerical solution of hyperbolic differential equations in cases where jump discontinuities exist, adaptive-stencil finite difference schemes provide a more stable and accurate alternative to fixed-stencil schemes. In practice, ENO and WENO schemes are very robust and the ESWENO scheme extends the WENO methodology by guaranteeing long-time stability in the energy norm. In this Thesis, we present the formulations of ENO, WENO, and ESWENO schemes and present the results via these schemes for numerical solution of several hyperbolic equations. These results display the ability of adaptive-stencil schemes to facilitate high-order accurate solutions to one- and two-dimensional linear and nonlinear hyperbolic equations where fixed-stencil schemes either display notable dispersive errors or excessive diffusive errors.

BIBLIOGRAPHY

[1] Gibbs, J. W., Fourier's Series, *Nature*, **59**:606–606 (1898).

[2] Gibbs, J. W., Fourier's Series, *Nature*, **59**:200–200 (1899).

[3] MacCormack, R. W., The Effect of Viscosity in Hypervelocity Impact Catering, AIAA Paper 69-354, 1969.

[4] Drummond, J. P., Diskin, G., Cutler, A., and Danehy, P., Fuel-Air Mixing and Combustion in Scramjets, AIAA Paper 2002-3878, 2002.

[5] Dimotakis, P. E., Turbulent Free Shear Layer Mixing and Combustion, in Murthy, S. N. B. and Curran, E. T., editors, *High Speed Flight Propulsion Systems*, *Progress in Astronautics and Aeronautics*, Vol. 137, Chapter 5, pp. 265–340, AIAA Publishing Co., Washington, D.C., 1991.

[6] Shu, C.-W., High Order Weighted Essentially Non-Oscillatory Schemes for Convection Dominated Problems, *SIAM Rev.*, **51**(1):82–126 (2009).

[7] Borges, R., Carmona, M., Costa, B., and Don, W. S., An Improved Weighted Essentially Non-Oscillatory Scheme for Hyperbolic Conservation Laws, *J. Comput. Phys.*, **227**(6):3191–3211 (2008).

[8] Burger, R. and Kozakevicius, A., Adaptive Multiresolution WENO Schemes for Multi-Species Kinematic Flow Models, *J. Comput. Phys.*, **224**(2):1190–1222 (2007).

[9] Chou, C.-S. and Shu, C.-W., High Order Residual Distribution Conservative Finite Difference WENO Schemes for Convection-Diffusion Steady State Problems on Non-Smooth Meshes, *J. Comput. Phys.*, **224**(2):992–1020 (2007).

[10] Harten, A., Engquist, B., Osher, S., and Chakravarthy, S. R., Uniformly high Order Accurate Essentially Non-Oscillatory Schemes, III, *J. Comput. Phys.*, **131**(1):3–47 (1987).

[11] Liu, X.-D., Osher, S., and Chan, T., Weighted Essentially Non-Oscillatory Schemes, *J. Comput. Phys.*, **115**(1):200–212 (1994).

[12] Jiang, G.-S. and Shu, C.-W., Efficient Implementation of Weighted ENO Schemes, *J. Comput. Phys.*, **126**(1):202–228 (1996).

[13] Yamaleev, N. and Carpenter, M., Third-order Energy Stable WENO Scheme, *J. Comput. Phys.*, **228**(8):3025–3047 (2009).

[14] Shu, C.-W., Essentially Non-Oscillatory and Weighted Essentially Non-Oscillatory Schemes for Hyperbolic Conservation Laws, in *Advanced Numerical Approximation of Nonlinear Hyperbolic Equations*, Chapter 4, pp. 325–432, Springer, New York, NY, 1998.

[15] LeVeque, R. J., *Finite Volume Methods for Hyperbolic Problems*, Cambridge University Press, Cambridge, UK, 2002.

[16] Richtmyer, R. and Morton, K., *Difference Methods for Initial-Value Problems, 2nd ed.*, Interscience, New York, NY, 1967.

[17] Harten, A., Lax, P. D., and van Leer, B., On Upstream Differencing and Godunov-Type Schemes for Hyperbolic Conservation Laws, *SIAM Rev.*, **25**(1):35–61 (1983).

[18] Kreiss, H.-O. and Scherer, G., Finite Element and Finite Difference Methods for Hyperbolic Partial Differential Equations, in *Mathematical Aspects of Finite Elements in Partial Differential Equations*, Academic Press, Inc., New York, NY, 1974.

[19] Strand, B., Summation by Parts for Finite Difference Approximations for d/dx, *J. Comput. Phys.*, **110**(1):47–67 (1994).

[20] Yamaleev, N. and Carpenter, M., A Systematic Methodology for Constructing High-order Energy Stable WENO Schemes, *J. Comput. Phys.*, **228**(11):4248–4272 (2009).

[21] Fisher, T., Carpenter, M., Yamaleev, N., and Frankel, S., Boundary Closures for Fourth-order Energy Stable Weighted Essentially Non-Oscillatory Finite Difference Schemes, NASA TM 2009-216166, NASA Langley Research Center, Hampton, VA, 2009.

[22] Courant, R., Friedrichs, K., and Lewy, H., On the Partial Difference Equations of Mathematical Physics, *IBM J. Res. Dev.*, **11**(2):215–234, English translation of the 1928 German original (1967).

[23] Burgers, J., *The Non-Linear Diffusion Equation: Asymptotic Solutions and Statistical Problems*, Springer, Boston, MA, 1974.